SPECTROSCOPIC CHARACTERIZATION, HIRSHFELD SURFACE, DFT, AND TD-DFT OF *tert*-BUTYL PHENETHYLCARBAMATE AND 1,1-DIMETHYL-3-PHENETHYLUREA**

M. B. Alshammari [1*], E. H. Anouar [1], G. A. El-Hiti [2]

[1] Department of Chemistry, College of Science and Humanities Studies in Al-Kharj, Prince Sattam Bin Abdulaziz University, Al-Kharj 11942, Saudi Arabia; e-mail: m.alshammari@psau.edu.sa, anouarelhassane@yahoo.fr
[2] Cornea Research Chair, Department of Optometry, College of Applied Medical Sciences, King Saud University, P.O. Box 10219, Riyadh 11433, Saudi Arabia; e-mail: gelhiti@ksu.edu.sa

*Tert-butylphenethylcarbamate (**1**) and 1,1-dimethyl-3-phenethylurea (**2**) were synthesized, and their structures were confirmed by NMR, FTIR, and mass spectrometry techniques. The experimental spectroscopic data of **1** and **2** were compared with the corresponding calculated ones obtained by density functional theory (DFT) and time-dependent DFT methods, for which the hybrid functionals B3LYP, B3P86, and PBE0 combined with the 6-311++G(d,p) basis set were tested. The solvent effect was considered using the implicit model – integral equation formalism-polarizable continuum model (IEFPCM). Relatively good correlation (R^2 > 90%) was obtained between the experimental and predicted spectral data. The conformational effect on the absorption maximum λ_{max} was negligible, that is, λ_{max} of different conformers varied by less than 0.01 nm. Hirshfeld surface analysis and electrostatic potential calculations of the closest intermolecular contacts between active atoms of **1** and **2** revealed that the closest interactions were between hydrogen atoms of 39.6 and 46.3%, respectively.*

Keywords: *time-dependent density functional theory, nuclear magnetic resonance, conformational analysis, tert-butylphenethylcarbamate, 1,1-dimethyl-3-phenethylurea.*

СПЕКТРОСКОПИЧЕСКАЯ ХАРАКТЕРИЗАЦИЯ, ПОВЕРХНОСТЬ ХИРШФЕЛЬДА, РАСЧЕТЫ МЕТОДАМИ DFT И TD-DFT *трет*-БУТИЛФЕНЭТИЛКАРБАМАТА И 1,1-ДИМЕТИЛ-3-ФЕНЭТИЛМОЧЕВИНЫ

M. B. Alshammari [1*], E. H. Anouar [1], G. A. El-Hiti [2]

УДК 539.143.43

[1] Колледж естественных и гуманитарных наук в Аль-Харже, Университет принца Саттама Ибн Абдель Азиза, Аль-Хардж 11942, Саудовская Аравия; e-mail: m.alshammari@psau.edu.sa; anouarelhassane@yahoo.fr
[2] Колледж прикладных медицинских наук, Университет короля Сауда, 10219, Эр-Рияд 11433, Саудовская Аравия; e-mail: gelhiti@ksu.edu.sa

(Поступила 9 апреля 2019)

*Синтезированы трет-бутилфенилэтилкарбамат (**1**) и 1,1-диметил-3-фенэтилмочевина (**2**), их структуры подтверждены методами ЯМР, ИК-Фурье- и масс-спектрометрии. Проведено сравнение эспериментальных результатов с соответствующими расчетными данными, полученными методами теории функционала плотности (DFT) и нестационарной теории DFT, для которых протестированы гибридные функционалы B3LYP, B3P86 и PBE0 совместно с базисным набором 6-311++G(d,p). Влияние растворителя рассмотрено с использованием имплицитной модели — формализма интегральных уравнений и модели поляризуемого континуума (IEFPCM). Получена сравни-*

** Full text is published in JAS V. 87, No. 4 (http://springer.com/journal/10812) and in electronic version of ZhPS V. 87, No. 4 (http://www.elibrary.ru/title_about.asp?id=7318; sales@elibrary.ru).

*тельно неплохая корреляция экспериментальных и расчетных спектральных данных (R^2 > 90%). Конформационное влияние на максимум поглощения λ_{max} незначительное, λ_{max} разных конформеров изменялось менее чем на 0.01 нм. Анализ поверхности Хиршфельда и расчеты электростатического потенциала ближайших межмолекулярных контактов между активными атомами **1** и **2** показывают наиболее близкие взаимодействия между атомами водорода 39.6 и 46.3%.*

Ключевые слова: *нестационарная теория функционала плотности, ядерный магнитный резонанс, конформационный анализ, трет-бутилфенэтилкарбамат, 1,1-диметил-3-фенэтилмочевина.*

Introduction. Compounds containing both carbamate [1–3] and urea [4–6] moieties have always generated interest because they show a variety of biological activities. The most common methods of producing carbamate involve reactions between *tert*-butyloxycarbonyl benzotriazoles and amino acids [7], oxopyridazine and amines [8], di-*tert*-butyl dicarbonate and nitriles [9] or carboxylic acids [10], as well as chloroformates and nitro compounds [11]. Moreover, several efficient approaches for the synthesis of urea derivatives have been developed [12–14]. Aromatic carbamates and urea can be substituted efficiently by treatment with organolithium reagents followed by reactions with electrophiles [15–20].

Quantum chemical calculations are powerful tools for the confirmation of experimental ^{1}H and ^{13}C NMR chemical shifts [21–23] and UV-visible absorption bands [24–26]. The excited states may be calculated using different approaches [25–32]. Previous studies reported that B3LYP and PBE0 are appropriate hybrid functionals for the estimation of excited state energies [33–37]. Previously, we showed that B3P86 and B3LYP provide reliable estimates of the first excited state of a series of flavonoids and chalcones [38]. Lumpi et al. reported that M06-2X gave more accurate predictions of the absorption and emission spectra of oligothiophene-based compounds than PBE0 and B3LYP [39]. To predict the UV-visible spectra of pyranoanthocyanins, Quartarolo and Russo [28] performed time-dependent density functional theory (TD-DFT) calculations with the PBE0 hybrid functional in the gas and solvent [conductor-like polarizable continuum model (C-PCM)] phases, and ab initio multi-reference coupled cluster calculations with the resolution of identity approximation to predict electronic spectra of pyranoanthocyanin. They concluded that the use of large basis sets does not significantly improve the predicted excitation energies, and the conformation of pyranoanthocyanin has a slight influence on the absorption maximum λ_{max} (i.e., the Boltzmann-weighted average of λ_{max} and λ_{max} of the stable conformer are similar) [28]. Sousa et al. tested the performance of pure hybrid functionals, B3LYP and PBE0, and long-range-corrected hybrid functionals, ωB97X and ωB97XD, in predicting the electronic absorption spectra of isopentaphyrin and its lutetium complex [29]. They found that the reproduction of absorption bands depends on the type of absorption band (e.g., the lowest excitation energy band for free isopentaphyrin was well predicted by ωB97XD) [29]. The gauge-independent atomic orbital (GIAO) method is the most common approach used to calculate the nuclear magnetic shielding tensors (σ_{iso}), and thus, to predict ^{1}H and ^{13}C NMR chemical shifts [40, 41].

We performed the synthesis and spectroscopic characterization of *tert*-butylphenethylcarbamate (**1**) and 1,1-dimethyl-3-phenethylurea (**2**)

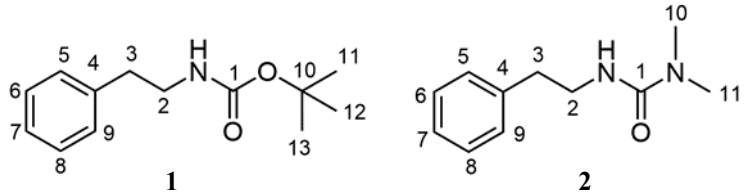

1 **2**

The spectroscopic data are compared with theoretical predictions by DFT and TD-DFT. The conformational effect on the λ_{max} of **1** and **2** was investigated by TD-DFT using the B3LYP hybrid functional. In addition, internal and external intermolecular contacts between active atoms of **1** and **2** were identified by analyzing Hirshfeld surface and electrostatic potential (ESP) maps.

Experimental. ^{1}H (400 MHz) and ^{13}C NMR (100 MHz) spectra were recorded on a Bruker AV400 NMR spectrometer. Mass spectra were recorded on a Waters GCT Premier mass spectrometer, with the accurate mass of the molecular ion peak determined using a Waters LCT Premier XE time-of-flight mass spectrometer. IR spectra (4000–400 cm^{-1}) were recorded on a Perkin-Elmer Spectrum Two FT-IR spectrometer.

*Synthesis of **1***. Di-*tert*-butyl dicarbonate (2.16 g, 9.91 mmol) was slowly added over a 5-min period to a stirred solution of 2-phenylethanamine (1.0 g, 8.26 mmol) in dichloromethane (10 mL) containing triethylamine (1.25 g, 12.39 mmol). The mixture was refluxed for 1 h, allowed to cool to room temperature, and then

poured onto H_2O (15 mL). The organic layer was separated, washed with H_2O (2×10 mL), and dried with $MgSO_4$, and the solvent was then removed under reduced pressure. The solid obtained was purified by crystallization from hexane to give pure **1** as colorless crystals (yield: 1.70 g, 7.68 mmol, 93%): mp 68–72°C; FTIR (cm^{-1}): 3376, 3065, 3029, 2979, 2934, 1686, 1520, 1497, 1161; ^{1}H NMR (500 MHz, $CDCl_3$): δ 7.33 (*t*, *J* = 7.5 Hz, 2H, H-3/H-5 of Ph), 7.28–7.21 (*m*, 3H, H-2/H-6 and H4 of Ph), 4.59 (*br s*, exch., 1H, NH), 3.41 (*q*, *J* = 7 Hz, 2H, CH_2NH), 2.82 (*t*, *J* = 7 Hz, 2H, CH_2Ar), 1.46 [s, 9H, $C(CH_3)_3$]; ^{13}C NMR (125 MHz, $CDCl_3$): δ 155.9 (*s*, C=O), 139.0 (*s*, C-1), 128.8 (*d*, C-3/C-5), 128.6 (*d*, C-2/C-6), 126.4 (*d*, C-4), 79.2 [*s*, $C(CH_3)_3$], 41.9 (*t*, CH_2NH), 36.3 (*t*, CH_2Ar), 28.6 [*q*, $C(CH_3)_3$]; MS (ES+): *m*/*z* (%) 465 (51, $[2M + Na]^+$), 285 (99, $[M + MeCNNa]^+$), 244 (100, $[M + Na]^+$), 229 (18), 188 (18), 105 (22); HRMS (ES+): *m*/*z* ($[M + Na]^+$) calcd for $C_{13}H_{19}NO_2$ 23Na: 244.1313; found: 244.1304.

Synthesis of ***2***. A mixture of 2-phenylethanamine (1.04 g, 8.58 mmol), dimethylcarbamoyl chloride (1.04 g, 9.65 mmol), and triethylamine (1.20 g, 1.18 mmol) in dichloromethane (10 mL) was refluxed for 1 h. The solid obtained upon cooling was collected by filtration, washed with H_2O (2×10 mL), and recrystallized from ethyl acetate and diethyl ether (1:3, v/v) to give pure **2** as colorless crystals (yield: 1.63 g, 8.48 mmol, 99%): mp 89–90°C, lit. 81–82°C [5], 88–90°C [17]; FT-IR (cm^{-1}): 3326, 3064, 3026, 2982, 2931, 1630, 1533, 1496, 903; ^{1}H NMR (500 MHz, $CDCl_3$): δ 7.32–7.19 (*m*, 5H, C_6H_5), 4.38 (*br*, exch., 1H, NH), 3.48 (app *q*, *J* = 7 Hz, 2H, C*H*$_2$NH), 2.85 [*s*, 6H, $N(CH_3)_2$], 2.82 (*t*, *J* = 7 Hz, 2H, $CH_2C_6H_5$); ^{13}C NMR (125 MHz, $CDCl_3$): δ 158.3 (*s*, C=O), 139.5 (*s*, C-1), 128.8 (*d*, C-3/C-5), 128.5 (*d*, C-2/C-6), 126.3 (*d*, C-4), 42.1 (*t*, CH_2NH), 36.5 (*t*, $CH_2C_6H_5$), 36.1 [*q*, $N(CH_3)_2$]; MS (EI): *m*/*z* (%) 192 (29, $[M]^+$), 147 (8), 101 (42), 72 (100); HRMS (EI): *m*/*z* $[M]^+$ calcd for $C_{11}H_{16}N_2O$: 192.1263; found: 192.1260.

Computational methods. The optimization of the ground-state geometry and frequency analysis of **1** and **2** were carried out using three hybrid functionals B3LYP, B3P86, and PBE0, combined with the 6-311++G(*d*,*p*) basis set [42]. True minima were confirmed by the absence of imaginary frequencies. The excited singlet state energies were calculated using the TD-DFT method and by considering the vertical approximation, i.e., the excited state (ES) energies were evaluated from the optimized GS geometries (Fig. 1). The λ_{max}, vertical electronic excitation energies ($E_{vert(abs)}$), and oscillator strength ($f > 0$ for allowed transition) were also calculated [27, 43].

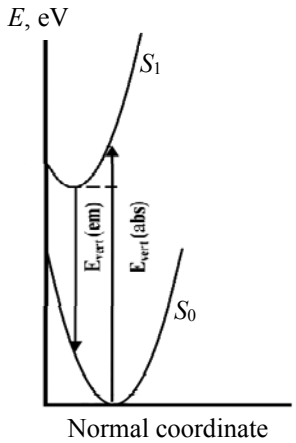

Fig. 1. Schematic representation of the vertical electronic transitions between GS (S_0) and ES (S_1).

The predicted ^{1}H and ^{13}C NMR magnetic isotropic shielding tensors (σ) were calculated by the standard GIAO approach [22] using B3LYP. The isotropic shielding constant σ_{iso} was used to calculate the isotropic chemical shift δ_{iso} with respect to tetramethylsilane using the equation $\delta_{iso}(X) = \sigma_{TMS}(X) - \sigma_{iso}(X)$. The predicted chemical shift δ_{pred} was calculated using the equation $\delta_{Pred} = a\delta_{Iso} + b$, where a and b are the slope and the intercept of the linear correlation curve between the calculated and experimental chemical shifts, respectively. The solvent effect was considered implicitly using PCM [44]. In this model, the solute is embedded in a shape-adapted cavity surrounded by a continuum solvent described by its dielectric constant ($\varepsilon_{methanol}$ = = 32.613 and $\varepsilon_{chlroform}$ = 4.7113). PCM has been reported to correctly model major solvent effects, including the electrostatic effect of a medium providing nonspecific solute-solvent interactions, such as hydrogen bond, dipole-dipole, or induced dipole-dipole interactions [45]. Liu et al. showed that dipole-dipole interac-

tions between coumarin and solvent molecules cause large red shifts [46]. For excited-state energy or TD-DFT calculations, the solvent effect was considered using the integral equation formalism (IEF)-PCM [47, 48]. We previously tested IEF-PCM and SS-PCM models for the prediction of the λ_{max} of terrein stereoisomers using different hybrid functionals, and the results confirmed that the combination of the state-specific PCM formalism with the M06-2X hybrid functional yields reliable excited-state predictions [39]. All theoretical calculations were performed using the Gaussian 09 package [49].

Hirshfeld surface and ESP analyses. Hirshfeld surface and fingerprint plots of **1** and **2** were obtained using Crystal Explorer 3.0 software [42]. The d_{norm} plots were mapped using a color scale ranging from blue (–0.51 a. u.) to red (1.34 a. u.). The red regions on the Hirshfeld surface indicate intermolecular hydrogen bonding interactions. The 2D fingerprint plots were expanded to cover a distance range of 0.6–2.8 Å. ESP surfaces were calculated by DFT at the level of the B3LYP/6-31+G(*d*,*p*) theory.

Results and discussion. *UV-visible spectroscopy*. The experimental and calculated λ_{max} for **1** and **2** and their corresponding intensities are summarized in Table 1. Experimentally, both compounds absorb at 259 nm. The calculated λ_{max} values for **1** and **2** correspond mainly to the HOMO→LUMO electronic transition, whose contribution is higher than 50%. The conformational effect on the λ_{max} shift was determined by calculating the excited states of stable conformers of **1**. Conformational analysis of **1** revealed the existence of five stable conformers. The λ_{max} values of the conformers slightly differ from each other, with the variation being less than 0.01 nm for the most stable conformers (Table 1). Hence, only the stable conformers of **1** and **2** were considered in the λ_{max} calculations using the B3P86 and PBE0 hybrid functionals. The λ_{max} values for **1** and **2** are underestimated by these hybrid functionals. The calculated excited states of **2** display a bathochromic shift in λ_{max} unlike those of **1** owing mainly to the greater delocalization in **2** compared with that in **1** [22].

TABLE 1. Experimental and Calculated Absorption Maximum λ_{max} (nm), Vertical Energy E_{max} (eV), Oscillator Strength *f*, and Absorbance of **1** and **2**

Method	Calculated (6-311++G(*d*,*p*) basis set and IEF-PCM)			Experimental		
	λ_{max}	E_{max}	*f*	λ_{max}	E_{max}	Absorbance
Compound **1**						
B3LYP				259	4.80	0.32
Conformer 1	219.31	5.65	0.09			
Conformer 2	219.31	5.65	0.09			
Conformer 3	219.32	5.65	0.09			
Conformer 4	217.78	5.69	0.15			
Conformer 5	218.00	5.69	0.13			
X-ray structure[a]	229.65	5.40	0.07			
B3P86	215.12	5.76	0.09			
PBE0	211.55	5.86	0.10			
Compound **2**						
B3LYP	231.71	5.35	0.03	259	4.80	0.31
B3P86	230.66	5.37	0.02			
PBE0	222.09	5.58	0.04			

[a] X-ray coordinates of the compounds were used to predict the absorption bands.

NMR characterization. The experimental and calculated ^{1}H and ^{13}C NMR chemical shifts of **1** and **2** are displayed in Table 2. The chemical shifts were calculated in the solvent phase at the B3LYP/6-311++G(*d*,*p*) level through the GIAO approach. Experimentally, the ^{1}H NMR chemical shifts of the methyl groups of **1** and **2** are observed at 1.46 and 2.85 ppm, respectively, while the predicted values are 1.46 and 2.68 ppm, respectively.

The downfield shift in **2** compared to that in **1** is mainly due to a higher electronegativity of nitrogen compared with carbon. Generally, the ^{1}H NMR and ^{13}C NMR chemical shifts of **1** and **2** are relatively well reproduced. The correlation coefficients (R^2) between the predicted and experimental ^{1}H NMR chemical shifts of **1** and **2** are 98.12 and 95.54%, respectively, while those between the predicted and experimental

^{13}C NMR chemical shifts of **1** and **2** are both 99.75%. For instance, the standard deviations in the ^{13}C NMR chemical shifts of the carbonyl (C=O) groups of **1** and **2** are 1.87 and 2.16 ppm, respectively.

TABLE 2. Experimental and Predicted Chemical Shifts (ppm) of **1** and **2**

Group	Compound **1**		Compound **2**	
	Calculated[a]	Experimental	Calculated	Experimental
^{1}H NMR				
$CH_2C_6H_5$	2.73	2.82	2.81	2.82
CH2NH	3.97	3.41	4.14	3.48
NH	4.13	4.59	4.00	4.38
$C(CH_3)_3$	1.46	1.46	—	—
$N(CH_3)_2$	—	—	2.68	2.85
H2/H6 and H4	7.24	7.33	—	—
H3/H5	7.36	7.28	7.22	7.32
$CH_2C_6H_5$	2.73	2.82	—	—
^{13}C NMR				
CO	154.0	155.90	156.14	158.30
C1	141.5	139.00	142.91	139.50
C2/C6	128.0	128.80	128.74	128.50
C3/C5	127.9	128.60	127.75	128.80
C4	125.1	126.40	125.61	126.30
CH_2NH	43.7	41.90	44.24	42.10
$CH_2C_6H_5$	38.4	36.30	38.23	36.50
$COOC(CH_3)_3$	82.1	79.20	—	—
$C(CH_3)_3$	24.0	28.60	—	—
$N(CH_3)_2$	—	—	32.52	36.10

[a] B3LYP/6-311++G(*d*,*p*) in the IEF-PCM solvent model.

FTIR characterization. FT-IR spectra of **1** and **2** are shown in Fig. 2. The main experimental and calculated vibrational modes of **1** and **2** are presented in Tables 3 and 4. The calculated vibrational modes are obtained at B3LYP/6-311++G(*d*,*p*), B3P86/6-311++G(*d*,*p*), and PBE0/6-311++G(*d*,*p*) levels of the theories. The calculated values are scaled with a factor of 0.9613. The stretching vibration mode N-H ($\nu_{N\text{-}H}$) of **1** and **2** is observed at 3376 and 3326 cm^{-1}, respectively (Fig. 2). All the tested hybrid functionals failed in the reproduction of $\nu_{N\text{-}H}$ of **1** and **2** with a standard deviation higher than 139 cm^{-1} (Table 3). The stretching vibration of the C-H bond of the aromatic ring ($\nu_{C\text{-}H}$, Ar) in compounds **1** and **2** appeared at 3065 and 3064 cm^{-1}, respectively. The stretching CH vibrations for aromatic compounds have been reported to appear within the region of 3100–3000 cm^{-1} [50]. Somehow, the $\nu_{C\text{-}H}$ of the aromatic ring of **1** is well reproduced with all the tested hybrid functionals with standard deviations of 11, 2, and 12 cm^{-1} for B3LYP, B3P86, and PBE0, respectively. All the tested hybrid functionals failed in the reproduction $\nu_{C\text{-}H}$ of the aro matic ring of **1**. However, this vibration is relatively well reproduced in **2** by using B3LYP and PBE0 with deviations of 21 and 15 cm^{-1}, respectively. The mean average deviation, maximal deviation, and minimal deviation between the experimental and scaled calculated vibrational modes of **1** and **2** are shown in Table 3.

It is obvious from Table 3 that the reproduction of the observed vibrational modes may depend on the type of vibration modes itself and the atoms involved in the 3D molecular structure and the tested hybrid functional. For instance, the ν_{CO} vibration of **1** and **2** appears at 1686 and 1630 cm^{-1}. The values are relatively well reproduced with B3P86 and PBE0 with standard deviations of less than 10 cm^{-1} (Table 3), while they are overestimated by B3LYP with shifts of 31 and 35 cm^{-1} for compounds **1** and **2**, respectively. The minimum deviation between the experimental and calculated vibrational modes of **1** is obtained for C-O bonds of the ester group with $\Delta\nu$ of 1 cm^{-1}, and it is obtained with the B3P86 hybrid functional, while for **2**, the minimum deviation is obtained for C-H bonds of the –CH_2-Ar group with $\Delta\nu$ of 1 cm^{-1}.

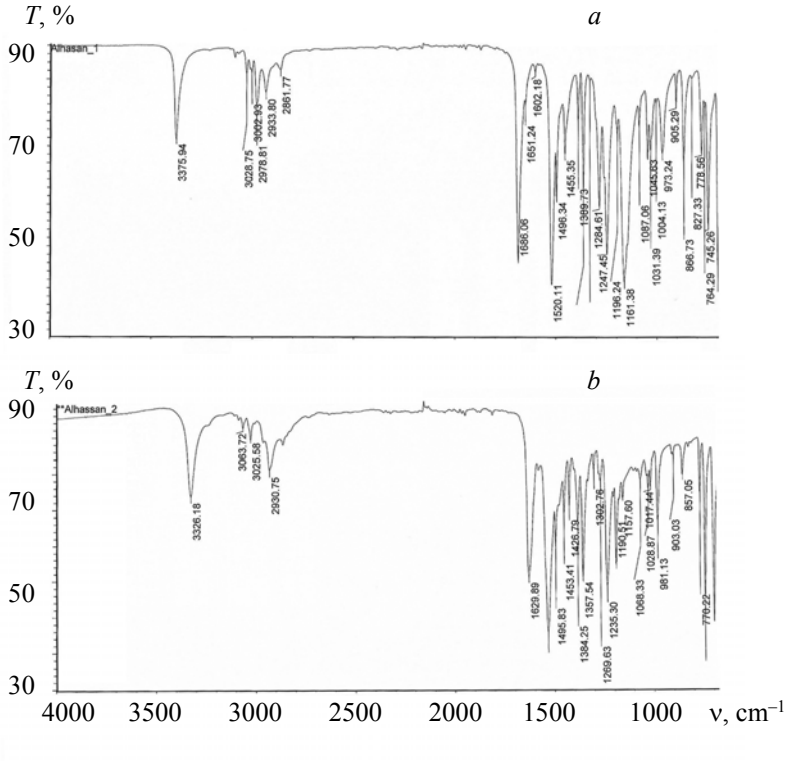

Fig. 2. FTIR spectrum of **1** (a) and **2** (b).

TABLE 3. Main Experimental and Scaled Calculated Vibrational Modes of Compounds **1** and **2**

Vibrational modes	Calculated, cm^{-1}			Exp, cm^{-1}	$\Delta\nu_{Exp-Scal}$, cm^{-1}		
	B3LYP	B3P86	PBE0		B3LYP	B3P86	PBE0
Compound 1							
ν_{N-H}	3515	3533	3549	3376	–139	–157	–173
ν_{C-H} (Ar)	3054	3067	3077	3065	11	–2	–12
ν_{C-H} (CH_3)	2937	2949	2956	3029	16	61	50
ν_{C-H} (-CH_2-NH-)	3013	2968	2979	2979	43	28	18
ν_{C-H} (-CH_2-Ar)	2936	2951	2961	2934	–3	–15	–22
$\nu_{C=O}$	1655	1683	1699	1686	31	3	–13
$\nu_{C=C}$ (Ar)	1566	1583	1482	1520	–46	-63	38
ν_{C-N} (N-$COO(CH_3)_3$	1488	1496	1505	1497	9	1	–8
ν_{C-O} $COOC(CH_3)_3$	1105	1167	1140	1161	56	–6	21
MAE					39	37	39
Max Div					139	157	173
Min Div					3	1	8
Compound 2							
ν_{N-H}	3526	3537	3554	3326	–200	–211	–228
ν_{C-H} (Ar)	3085	3100	3079	3064	–21	–36	–15
ν_{C-H} (CH_3)	2907	2913	2931	3026	9	–7	–16
ν_{C-H} (-CH_2-NH-)	3017	3033	3042	2982	–1	-19	–31
ν_{C-H} (-CH_2-Ar)	2983	3001	3013	2931	24	18	0
$\nu_{C=O}$	1595	1624	1640	1630	35	6	–10
$\nu_{C=C}$ (Ar)	1565	1582	1613	1533	–32	–49	–80
ν_{C-N}	1500	1609	1520	1496	–4	–113	–24
ν_{C-C}, (Ar-C-C-NH-)	932	942	947	903	–29	–39	–44
MAE					39	55	50
Max Div					200	211	228
Min Div					1	6	0

Hirshfeld surface and ESP analyses. Hirshfeld surfaces of **1** and **2** mapped over d_{norm}, shape index, and curvedness were obtained using Crystal Explorer 3.0 (Fig. 3). The internal and external contact distances (d_i and d_e, respectively) from the Hirshfeld surface to the nearest atom inside and outside enable analysis of intermolecular interactions through the mapping over d_{norm}.

The red regions on the Hirshfeld surface indicate the existence of intermolecular interactions (intercontacts) in the crystalline environment (Fig. 4). As shown on the Hirshfeld surface mapped over d_{norm}, this active region is near the oxygen atom of the carbonyl group and the hydrogen atom of the amide group (Fig. 4). The intermolecular hydrogen bonding interactions between the receptors and donors in compounds **1** and **2** are marked on the Hirshfeld surface by dotted lines in Fig. 4. The intermolecular hydrogen bond distances between the oxygen atom of the carbonyl group of the basic unit and hydrogen atom of the amide group of another unit are 2.286 and 2.060 Å for compounds **1** and **2**, respectively. ESPs were calculated by DFT at the B3LYP/6-31+G(*d*,*p*) level of the theory (Fig. 4). The negative region on the ESP (shown in red) is due to the hydrogen bond acceptor, while the positive region (shown in blue) is due to the hydrogen bond donor.

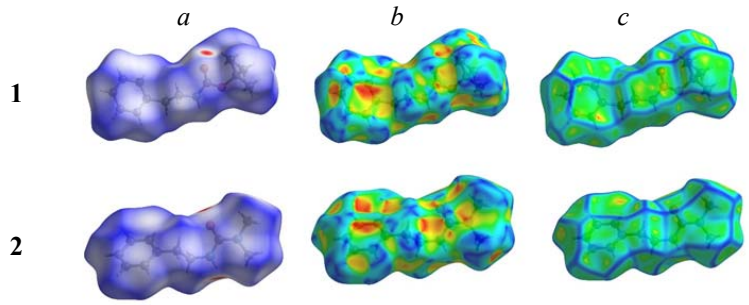

Fig. 3. Hirshfeld surfaces of **1** and **2** mapped over (a) d_{norm}, (b) shape index, and (c) curvedness.

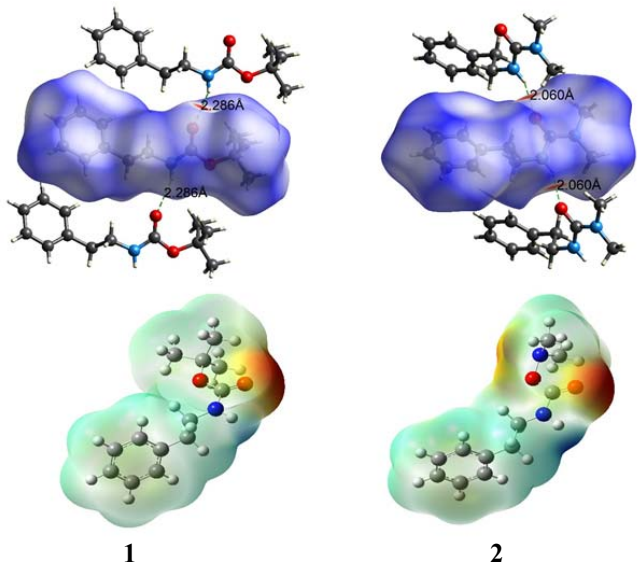

Fig. 4. Mapping of Hirshfeld surface over d_{norm} showing intermolecular hydrogen bonding interactions in **1** and **2** (top), and Electrostatic potentials of **1** and **2** obtained at the B3LYP/6-31+G(*d*,*p*) level of theory (bottom).

The two-dimensional fingerprint plots for the inter-contacts of **1** and **2** with large contributions to the Hirshfeld surface are shown in Fig. 5. The highest contributions to the Hirshfeld surfaces of **1** and **2** are 72.4 and 70.40%, respectively, from inter-contacts between hydrogen atoms (H···H).

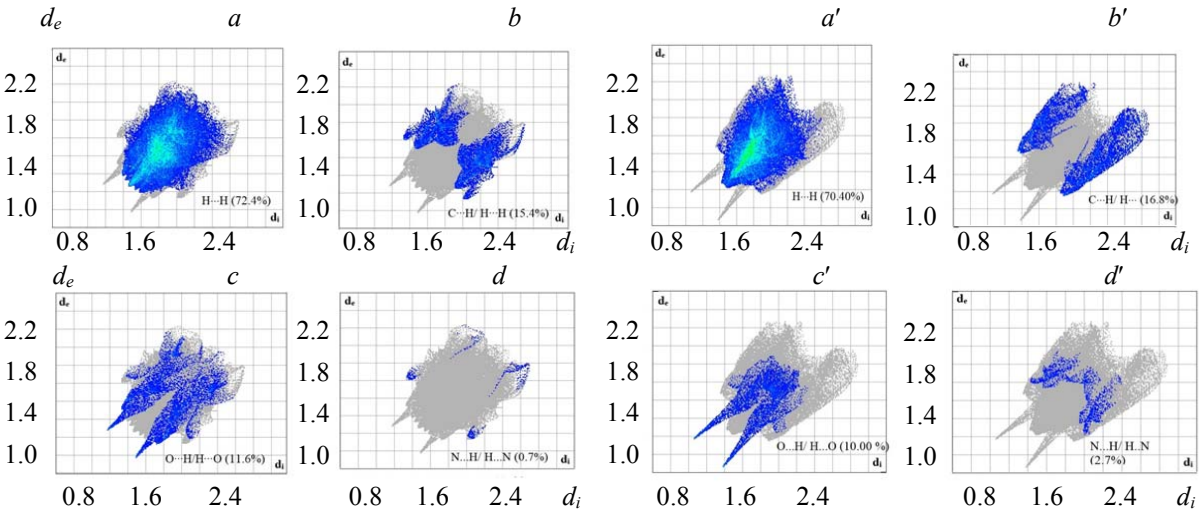

Fig. 5. Two-dimensional fingerprint plots of **1** (a–d) and **2** (a′–d′) showing contributions from (a, a′) H···H, (b, b′) C···H/H···C, (c, c′) O···H/H···O, and (d, d′) N···H/H···N contacts. The internal and external contact distances (d_i and d_e) are in Å.

Conclusions. The molecular structures of both *tert*-butylphenethylcarbamate and 1,1-dimethyl-3-phenethylurea were elucidated by various spectroscopic methods. Relatively good correlations were found between the experimental and calculated spectral data. The conformational study revealed the negligible effect of conformation on λ_{max} of **1**. The Hirshfeld surface and ESP analyses revealed an intercontact between the oxygen atom of the carbonyl group on one side and the hydrogen atom of the amide group on the other.

Acknowledgments. The authors extend their appreciation to the College of Science and Humanities Studies Research Centre and Deanship of Scientific Research at Prince Sattam bin Abdulaziz University for the funding of this research.

REFERENCES

1. M. Krátký, M. Volková, E. Novotná, E. Trejtnar, J. Stolaříková, J. Vinšová, *Bioorg. Med. Chem.*, **22**, 4073–4082 (2014).
2. Y. Yang, A. Voak, S. R. Wilkinson, L. Hu, *Bioorg. Med. Chem. Lett.*, **22**, 6583–6586 (2012).
3. A. Blaser, B. D. Palmer, H. S. Sutherland, I. Kmentova, S. G. Franzblau, B. Wan, Y. Wang, Z. Ma, A. M. Thompson, W. A. Denny, *J. Med. Chem.*, **55**, 312–326 (2012).
4. B. Kocyigit-Kaymakcioglu, A. O. Celen, N. Tabanca, A. Ali, S. I. Khan, I. A. Khan, D. E. Wedge, *Molecules*, **18**, 3562–3576 (2013).
5. A. A. Wilson, A. Garcia, S. Houle, O. Sadovski, N. Vasdev, *Chem. Eur. J.*, **17**, 259–264 (2011).
6. G. B. af Gennäs, L. Mologni, S. Ahmed, M. Rajaratnam, O. Marin, N. Lindholm, M. Viltadi, C. Gambacorti-Passerini, L. Scapozza, J. Yli-Kauhaluoma, *Chem. Med. Chem.*, **6**, 1680–1692 (2011).
7. T. S. Ibrahim, S. R. Tala, S. A. El-Feky, Z. K. Abdel-Samii, A. R. Katritzky, *Synlett*, **22**, 2013–2016 (2011).
8. H.-G. Lee, M.-J. Kim, S.-E. Park, J.-J. Kim, S.-G. Lee, Y.-J. Yoon, *Synlett*, 2809–2814 (2009).
9. S. Caddick, D. B. Judd, A. K. de K. Lewis, M. T. Reich, M. R. V. Williams, *Tetrahedron*, **59**, 5417–5423 (2003).
10. H. Lebel, O. Leogane, *Org. Lett.*, **8**, 5717–5720 (2006).
11. A. Porzelle, M. D. Woodrow, N. C. O. Tomkinson, *Synlett*, **5**, 798–802 (2009).
12. E. Artuso, I. Degani, R. Fochi, C. Magistris, *Synthesis*, **22**, 3497–3506 (2007).
13. T. Mizuno, T. Nakai, M. Mihara, *Synthesis*, **15**, 2492–2496 (2009).
14. K. Thalluri, S. R. Manne, D. Dev, B. Mandal, *J. Org. Chem.*, **79**, 3765–3775 (2014).
15. K. Smith, G. A. El-Hiti, M. B. Alshammari, *Synthesis*, **46**, 394–402 (2014).
16. K. Smith, G. A. El-Hiti, M. B. Alshammari, A. Fekri, *Synthesis*, **45**, 3426–3434 (2013).
17. K. Smith, G. A. El-Hiti, M. B. Alshammari, *Synthesis*, **44**, 2013–2022 (2012).

18. K. Smith, G. A. El-Hiti, M. B. Alshammari, *J. Org. Chem*., **77**, 11210–11215 (2012).
19. K. Smith, G. A. El-Hiti, A. S. Hegazy, *Synthesis*, **8**, 1371–1380 (2010).
20. K. Smith, G. A. El-Hiti, A. P. Shukla, *J. Chem. Soc., Perkin Trans.*, **1**, 2305–2313 (1999).
21. J. Gauss, *Chem. Phys. Lett*., **191**, 614–620 (1992).
22. J. Gauss, *J. Chem. Phys*., **99**, 3629–3643 (1993).
23. J. Gauss, *Ber. Bunsenges. Phys. Chem.,* **99**, 1001–1008 (1995).
24. K. L. Bak, A. E. Hansen, K. Ruud, T. Helgaker, J. Olsen, P. Jørgensen, *Theor. Chim. Acta*, **90** 441–458 (1995).
25. R. Bauernschmitt, R. Ahlrichs, *Chem. Phys. Lett*., **256**, 454–464 (1996).
26. M. E. Casida, C. Jamorski, K. C. Casida, D. R. Salahub, *J. Chem. Phys*., **108**, 4439–4449 (1998).
27. F. Furche, R. Ahlrichs, *J. Chem. Phys*., **117**, 7433–7447 (2002).
28. A. D. Quartarolo, N. Russo, *J. Chem. Theory Comput*., **7**, 1073–1081 (2011).
29. F. F. Ramos Sousa, A. D. Quartarolo, E. Sicilia, N. Russo, *J. Phys. Chem. B*, **116**, 10816–10823 (2012).
30. M. E. Alberto, B. C. De Simone, G. Mazzone, A. D. Quartarolo, N. Russo, *J. Chem. Theory Comput.*, **10**, 4006–4013 (2014).
31. M. E. Alberto, G. Mazzone, A. D. Quartarolo, F. F. R. Sousa, E. Sicilia, N. Russo, *J. Comput. Chem*., **35**, 2107–2113 (2014).
32. G. Mazzone, N. Russo, E. Sicilia, *Can. J. Chem*., **91**, 902–906 (2013).
33. D. Jacquemin, E. A. Perpète, G. E. Scuseria, I. Ciofini, C. Adamo, *J. Chem. Theory Comput*., **4**, 123–135 (2008).
34. D. Jacquemin, J. Preat, M. Charlot, V. Wathelet, J.-M. André, E. A. Perpetè, *J. Chem. Phys*., **121**, 1736–1743 (2004).
35. D. Jacquemin, J. Preat, V. Wathelet, M. Fontaine, E. A. Perpetè, *J. Am. Chem. Soc*., **128**, 2072–2083 (2006).
36. D. Jacquemin, V. Wathelet, J. Preat, E. A. Perpète, *Spectrochim. Acta A*, **67**, 334–341 (2007).
37. J. N. Woodford, *Chem. Phys. Lett*., **410**, 182–187 (2005).
38. E. H. Anouar, J. Gierschner, J.-L. Duroux, P. Trouillas, *Food Chem*., **131**, 79–89 (2012).
39. D. Lumpi, E. Horkel, F. Plasser, H. Lischka, J. Fröhlich, *Chem. Phys. Chem.*, **14**, 1016–1024 (2013).
40. K. Wolinski, J. F. Hinton, P. Pulay, *J. Am. Chem. Soc*., **112**, 8251–8260 (1990).
41. J. R. Cheeseman, G. W. Trucks, T. A. Keith, M. J. Frisch, *J. Chem. Phys*., **104**, 5497–5509 (1996).
42. A. D. Becke, *J. Chem. Phys*., **98**, 5648–5652 (1993).
43. G. Scalmani, M. J. Frisch, B. Mennucci, J. Tomasi, R. Cammi, V. Barone, *J. Chem. Phys*., **124**, 094107 (2006).
44. J. Tomasi, B. Mennucci, R. Cammi, *Chem. Rev*., **105**, 2999–3094 (2005).
45. D. Jacquemin, V. Wathelet, E. A. Perpète, C. Adamo, *J. Chem. Theory Comput*., **5**, 2420–2435 (2009).
46. X. Liu, J. M. Cole, K. S. Low, *J. Phys. Chem. C*, **117**, 14731–14741 (2013).
47. R. Improta, V. Barone, G. Scalmani, M. J. Frisch, *J. Chem. Phys*., **125**, 054103 (2006).
48. R. Improta, G. Scalmani, M. J. Frisch, V. Barone, *J. Chem. Phys*., **127**, 074504 (2007).
49. M. J. Frisch, G. W. Trucks, H. B. Schlegel, G. E. Scuseria, M. A. Robb, J. R. Cheeseman, G. Scalmani, V. Barone, G. A. Petersson, H. Nakatsuji, X. Li, M. Caricato, A. Marenich, J. Bloino, B. G. Janesko, R. Gomperts, B. Mennucci, H. P. Hratchian, J. V. Ortiz, A. F. Izmaylov, J. L. Sonnenberg, D. Williams-Young, F. Ding, F. Lipparini, F. Egidi, J. Goings, B. Peng, A. Petrone, T. Henderson, D. Ranasinghe, V. G. Zakrzewski, J. Gao, N. Rega, G. Zheng, W. Liang, M. Hada, M. Ehara, K. Toyota, R. Fukuda, J. Hasegawa, M. Ishida, T. Nakajima, Y. Honda, O. Kitao, H. Nakai, T. Vreven, K. Throssell, J. A. Montgomery, Jr., J. E. Peralta, F. Ogliaro, M. Bearpark, J. J. Heyd, E. Brothers, K. N. Kudin, V. N. Staroverov, T. Keith, R. Kobayashi, J. Normand, K. Raghavachari, A. Rendell, J. C. Burant, S. S. Iyengar, J. Tomasi, M. Cossi, J. M. Millam, M. Klene, C. Adamo, R. Cammi, J. W. Ochterski, R. L. Martin, K. Morokuma, O. Farkas, J. B. Foresman, D. J. Fox, *Gaussian 09, Revision A.1*, Gaussian, Wallingford CT (2009).
50. R. M. Silverstein, F. X. Webster, D. J. Kiemle, D. L. Bryce, *Spectrometric Identification of Organic Compounds*, John Wiley & Sons, New York (2015).